Chemical Physics Impact 11 (2025) 100931

Contents lists available at ScienceDirect

Chemical Physics Impact

journal homepage: www.sciencedirect.com/journal/chemical-physics-impact

Full length article

Efficient modeling of dynamic properties in K_3C_{60} using machine learning force fields

Ran Mo [a], Zhishuo Huang [b,a,*], Liviu Ungur [a,*]

[a] Department of Chemistry, National University of Singapore, 117543, Singapore
[b] Electrical Engineering and Computer Science, Technische Universität Berlin (TU Berlin), Germany

ARTICLE INFO

Dataset link: https://doi.org/10.24435/materialscloud:py-bf

Keywords:
Machine learning force field
Thermal-dynamics
Fullerides

ABSTRACT

Dynamic properties of the alkali-doped molecular crystal K_3C_{60} are investigated using machine learning force field (MLFF). Our trained force fields successfully reproduce phonons comparable to those from density functional theory 10-times faster in computational efficiency. Specific heat with MLFF also show good agreement with experimental data, demonstrating its reliability for thermodynamic analysis. Two descriptor schemes, Smooth Overlap of Atomic Positions and Atomic Cluster Expansion, are employed and systematically compared. This study represents the first detailed exploration of dynamic properties in molecular crystals using MLFF, highlighting MLFF's potential in more complex molecular crystals, such as C_{60} disorder in fullerides, molecular melting.

1. Introduction

Lattice dynamics is critical for understanding the fundamental thermal, mechanical, and electronic properties of crystalline materials [1–3]. At the heart of this field lies the study of phonons, quantized vibrational modes responsible for transmitting thermal energy in solids [4]. Phonon-related properties are particularly significant in materials science and condensed matter physics, where controlling lattice dynamics can enable the development of novel materials with tailored characteristics for specific applications. In the case of molecular crystals, lattice dynamics becomes even more intricate due to the weak elastic coupling between individual molecules, leading to unique dynamic properties that can result in exotic materials, of which there are many examples, including single molecular magnets [5], alkali-doped fullerides [6], and two-dimensional van der Waals (vdW) heterostructures [7].

Phonon calculations typically employ two main approaches: density functional theory (DFT) [8] and molecular dynamics (MD) [9–11]. While DFT-based phonon dispersion calculations are known for their accuracy, they are computationally expensive, scaling as $O(N^4)$ [12–14], with N representing the number of atoms in the system. Consequently, their application is limited to relatively simple crystals with smaller unit cells. In contrast, MD methods scale as O(N), making them more suitable for complex systems such as disordered materials, alloys, polymers, and interfaces. However, MD typically relies on empirical force fields, which may lack the accuracy needed for precise predictions, particularly for systems requiring quantum mechanical treatment. Recent advancements have aimed to improve MD accuracy by incorporating quantum mechanical insights into the force fields. Still, achieving a universally ideal force field potential remains challenging, as accurately partitioning the total electronic energy into atom–atom contributions (e.g., Coulombic, polarization, dispersion) is difficult [15]. Although various corrections (e.g., DFT+U [16–18] for the correction of Coulomb interaction, DFT+D [19,20] and vdW-DFT [21] for the non-long interaction correction, and relativistic calculations accounting for spin–orbit coupling (SOC)) can enhance DFT accuracy, they also increase computational costs.

The advent of artificial intelligence (AI) and machine learning (ML) techniques offers a promising alternative by combining the strengths of DFT and MD. Machine learning force field (MLFF) is a special case of application of artificial intelligence (AI), which significantly speeds up the derivation of the inter-atomic potentials (i.e., Force Field) compared to the derivation of classical force fields. The data required for the training process of MLFF are the structural information, energy, forces, and stress, which are the basic results in almost any first-principles calculations. For effective and accurate training of the MLFF, a large amount of data needs to be acquired or generated by computational means. Molecular dynamics is a good way to generate different structures of the same material, covering the most important part of the relevant structural configuration space. These potentials can accurately replicate DFT data and are considered more precise than traditional cluster functionals for generating key dynamic features for calculations, such as interatomic force constants (IFCs). These methods have shown significant potential across materials science, from

* Corresponding author.
E-mail addresses: zhishuohuang@gmail.com (Z. Huang), chmlu@nus.edu.sg (L. Ungur).

https://doi.org/10.1016/j.chphi.2025.100931
Received 30 May 2025; Received in revised form 9 August 2025; Accepted 21 August 2025
Available online 1 September 2025

predicting mechanical properties and thermal transport to designing atomistic potentials [22–26]. By training ML models on DFT-level data, it is possible to generate force fields that accurately reflect key interactions, including Coulomb and non-local vdW forces, thus enhancing the efficiency and applicability of MD simulations.

However, the power of ML are not directly based on physical or chemical principles, and their high accuracy thus comes at the expense of interpretability, often treating the training procedure as "black box" models [27]. On the other hand, applying them to complex materials, such as molecular crystals and heterostructures, presents additional challenges due to lower symmetry and increased atomic complexity. The alkali-doped fullerides A_3C_{60}, which adopt a face-centered cubic (FCC) structure, provide a suitable test case for ML methods due to their relatively high symmetry and weak long-range interactions. This material is known for its unusual electronic properties, including superconductivity in both equilibrium and non-equilibrium states and metal–insulator transitions that can be modulated by factors such as carrier concentration, pressure, and the type of alkali atom [28,29].

Our study aims to assess the applicability of MLFFs for investigating the lattice dynamics of molecular crystals, specifically alkali-doped fullerides. We also explore the potential of ML methods to reproduce phonon properties with computational efficiency while maintaining high accuracy, thereby offering a viable alternative for large-scale phonon calculations in more complex materials, such as the disorders of fullerenes. In this paper, we demonstrate the successful application of MLFF in predicting IFCs for K_3C_{60}, based on which the lattice dynamic properties of this material are studied. The MLFF are generated using two schemes, Smooth Overlap of Atomic Positions (SOAP) [30], and the Atomic Cluster Expansion (ACE) [27] schemes, for which a comparison is carried out.

2. Machine learning force field

For one crystal (with N atoms), its dynamic properties can be generated from the potential energy surface (PES), which is a function of three cartesian coordinates of each atom in one crystal (3N total degrees of freedom). The total energy can be expressed by the summation of the energy associated with each atom:

$$E = \sum_I E_I + V_e(conf), \tag{1}$$

where $V_e(conf)$ is the electron potential for one structure configuration. However, this method requires a detailed description of the structure: atomic species, the distances between atoms and their orientations, which is inconvenient when atoms are permuted, or the structure is translated or rotated. A more effective representation maps an atomic structure/configuration on a basis vector, which remains unchanged under permutation/translation/rotation operations. These basis vectors, named *descriptors*, form a feature space based on which the machine-learning engine can be constructed. Besides, with descriptors it becomes easier to systematically distinguish the similarity of structures, regress structure–property relationship, or analyze configuration space by lower-dimensional visualizations.

As one of the most common methods for describing the atomic structure (the other one is related to internal coordinates [31]), the decomposition of total energy can be expanded based on these atomic density distribution functions (ADDF) [32], expressed as:

$$\rho(\mathbf{r}) = \sum_i \omega_{Z_i} \delta(\mathbf{r} - \mathbf{r}_i), \tag{2}$$

where i indicates the neighboring atoms within some cutoff distance, ω_{Z_i} is a unique weight factor according to the atomic species i, and $\mathbf{r}_i$ is the vector from the central atom to neighbor i. Suppose all the species of atoms are treated as identical, $\omega_{Z_i} = 1$. This definition of ADDFs guarantees permutational and translational invariance. The rotational invariance will be fulfilled by introducing the basis set, which is defined in a similar way as that for the electronic part:

$$\phi_{nlm}(\mathbf{r}) = a_c R_{nl}(r) Y_{lm}(\hat{\mathbf{r}}), \tag{3}$$

where a_c is the coefficient, $\hat{\mathbf{r}} = \mathbf{r}/r$, $r = |\mathbf{r}|$, and $R_{nl}(r)$ and $Y_{lm}(\hat{\mathbf{r}})$ are for the radial part (polynomials) and the angular part (spherical harmonics) respectively. The descriptors are a collection of the projection coefficients of the ADDF onto the basis set:

$$c_{nlm} = \langle \rho(\mathbf{r}) | \phi_{nlm}(\mathbf{r}) \rangle . \tag{4}$$

With the definition of the basis set and descriptors, the training procedure can be performed for various methods; in this work, we employ an effective Gaussian regression method. The key point of training is not the descriptors (or structures) themselves but the similarity between the descriptors of two structures/configurations, which the kernel can characterize. This similarity measurement should also fulfill the requirement for the descriptors, which is the permutation rotation invariance; thus, the ADDF is a good candidate for constructing the kernels. The kernel technique solves a low-dimensional problem by adding additional dimensions. In material science, the kernel is a fixed (nonlinear) function to characterize the degree of similarity between the atomic environments described by its two arguments: ρ, ρ'. The most straightforward way [30] to characterize structure similarity is to calculate the inner product of two atomic neighbor densities as

$$S(\rho, \rho') = \int \rho(\mathbf{r}) \cdot \rho(\mathbf{r}) d\mathbf{r}. \tag{5}$$

Therefore, the kernel $k(\boldsymbol{\rho}, \boldsymbol{\rho}')$ can be interpreted as a covariance function, which must be symmetric and positive defined [30]. A good review of the kernel can be found in Rasmussen and Williams's book [33].

To comply with the requirement for permutational, rotational, and translational invariance, the kernel can be defined by integrating all rotational operations as follows:

$$k(\rho, \rho') = \int \left| S(\rho, \hat{\mathbf{R}}\rho') \right|^n d\hat{\mathbf{R}} = \int d\hat{\mathbf{R}} \left| \rho(\mathbf{r}) \rho(\hat{\mathbf{R}}\mathbf{r}) d\mathbf{r} \right|^n . \tag{6}$$

Finally, the trained model should be validated for further applications. Many attempts have been proposed to validate the MLFF. A systematic way and definition to validate the MLFF method was proposed [34,35], mainly focuses on three aspects:

- Intrinsic numerical error of the MLFF, which characterizes the intrinsic error between DFT calculation and MLFF during training,
- Comparison between DFT and MLFF after training, which characterizes how well MLFF can reproduce the DFT data for a given structure that is not far away from the initial structure,
- Comparison between MLFF and experimental data, which finally validates the MLFF training.

In this paper, we will follow this validation method.

2.1. Comparison between SOAP and ACE

In this paper, two MLFF schemes: Smooth Overlap of Atomic Positions (SOAP) proposed by A. P. Bartók [30], and the Atomic Cluster Expansion (ACE) generalized by R. Drautz [27], are employed, of which a full comparison of these two methods is shown in Table 1.

Regarding the radial part of the basis set ($R_{nl}(r)$), SOAP uses cubic and higher-order polynomials, while in ACE, the radial part is the described by the Chebyshev polynomials of the first kind [36]. Since these polynomials are complete basis sets, Chebyshev polynomials, and cubic and higher-order polynomials should be equivalent when high enough order of the radial parts of these basis sets are included; thus, the two basis sets of both ACE and SOAP schemes are equivalent to each other [27]. We should note that with a non-orthogonal basis set, this scheme can also be employed by including the overlap matrix $\mathbf{S}$. The angular part of these two schemes is expressed by the spherical

Table 1
Comparison between SOAP [30] and ACE [27] schemes, concerning the basis set (ϕ_{nlm}), descriptors ($\mathbf{p}$), and the kernel ($k(\rho,\rho')$).

		SOAP	ACE
$\phi_{nlm}(\mathbf{r})$	a_c	1	$\sqrt{4\pi}$
	$R_{nl}(r)$	$\sum_{\alpha=1}^{n_{\max}}(\mathbf{S}^{-1/2})_{n\alpha}\sqrt{\frac{2\alpha+5}{r_{\rm cut}^{2\alpha+5}}}(r_{\rm cut}-r)^{(\alpha+2)}$, $S_{n\alpha}=\frac{\sqrt{(5+2\alpha)(5+2n)}}{5+n+\alpha}$	$\sum_{k=1}\frac{1}{4}c_{nlk}\left[1-T_{k-1}(x)\right]\left[1+\cos\frac{\pi r}{r_c}\right]$ $(n>0\ \&\ n\geq l)$, $\begin{cases} T_0(x) & =1 \\ T_1(x) & =x \\ T_{n+1}(x) & =2xT_n(x)-T_{n-1}(x) \\ x & =1-2\frac{\exp(-\lambda(r/r_c-1))-1}{\exp(\lambda)-1} \end{cases}$
	$\hat{\mathbf{r}}$	$Y_{lm}(\hat{\mathbf{r}})$	
$\mathbf{p}$		$\begin{cases} \sum_{m=-l}^{l} c^*_{nlm}c_{nlm} \\ \sum_{m,m_1,m_2} c^*_{nlm}C^{ll_1l_2}_{mm_1m_2}c_{nl_1m_1}c_{nl_2m_2} \\ \sum_{m=-l}^{l} c^*_{n_1lm}c_{n_2lm} \\ \sum_{m,m_1,m_2} c^*_{n_1lm}C^{ll_1l_2}_{mm_1m_2}c_{n_2l_1m_1}c_{n_2l_2m_2} \end{cases}$	$\begin{cases} R_{n0}(r_{ij}) \\ \frac{1}{2l+1}\sum_{jk}R_{n_1l}(r_{ji})R_{n_2l}(r_{ki})P_l(\cos\theta_{jik}) \end{cases}$
$k(\rho,\rho')$		$k(\rho,\rho')=\left(\frac{k'(\rho,\rho')}{\sqrt{k'(\rho,\rho)k'(\rho',\rho')}}\right)^{\zeta}$, $\zeta=1,2,3,\ldots$, $\rho(\mathbf{r})=\sum_i\exp(-c_G\lvert\mathbf{r}-\mathbf{r}_i\rvert^2)$, $k'(\rho,\rho')=\begin{cases} \frac{8\pi^2}{2l+1}\sum_{n,n',l}p_{nn'l}p'_{nn'l}, & n=2 \\ \frac{8\pi^2}{2l+1}\sum_{\substack{n_1,n_2,n\\ l_1,l_2,l}}b_{n_1n_2nll_1l_2}b'_{n_1n_2nll_1l_2}, & n=3 \end{cases}$	$k(\sigma,\sigma')=1+\sum_{\gamma\nu}\Phi^*_{\gamma\nu}(\sigma)\Phi_{\gamma\nu}(\sigma')$, $\rho(\mathbf{r})=\sum_i\delta(\mathbf{r}-\mathbf{r}_i)$, $\Phi_{\alpha\nu}=\phi_{\upsilon_1}(\mathbf{r}_{j_1i})\phi_{\upsilon_2}(\mathbf{r}_{j_2i})\ldots\phi_{\upsilon_l}(\mathbf{r}_{j_li})$

harmonics ($Y_{lm}(\hat{\mathbf{r}})$). The descriptors used in MLFF training are obtained by projecting the ADDPs onto these basis sets (Eq. (4)). Despite the equivalent basis set, the perspective of representing structures in these two schemes differs. In SOAP, the structure is described by bond order parameters; a complete description of different structures involves the bond-order parameters (power spectrum (p_l) and bi-spectrum ($b_{l_1l_2}$) for second-order and third-order) to the third-order. In this case, the rotational invariance is fulfilled as any rotation operator corresponds to the Wigner matrices $\mathbf{D}^l(\hat{R})$, which form the irreducible representations of the three-dimensional rotation group SO(3). While in ACE, the technique of atomic cluster expansion function ($\Phi_{\alpha\nu}$) provides a systematic way to generate higher-order $B^{(n)}$ interactions by adjusting the expansion order, making it suitable for applications requiring highly accurate interatomic potentials and fitting potential energy surfaces.

The features of these basis sets and perspectives for representing structures determine the kernels $k(\rho,\rho')$. In SOAP kernel, local environments are characterized by calculating the smooth overlap of atomic density distributions, where the local density around each atom is represented by Gaussian functions instead of δ functions centered on its neighbors. While ACE is particularly advantageous for detailed interatomic potential fitting, SOAP excels in tasks that involve similarity-based analysis, such as clustering atomic structures or kernel-based machine learning models for predicting material properties.

3. Computational methods

The crystal constant of K_3C_{60} is 14.240 Å [37]. In the SOAP scheme, all DFT calculations, ab initio molecular dynamics, are carried out by VASP 6.3 [38,39]. The plane-wave kinetic energy cutoff is set to 1000 eV and a 4 × 4 × 4 Monkhorst–Pack (MP) mesh [40] is used to perform Brillouin zone (BZ) integration to ensure the convergence of DFT calculation. The convergence threshold of total energy is set to 10^{-6} eV. Projector augmented-wave(PAW) pseudo-potentials [41,42] are employed with the exchange and correlation approximations Generalized Gradient Approximation PBE (GGA-PBE) [43]. The Gaussian smearing of width 0.05 eV is used. The training data in the SOAP scheme is named VASPset. The MLFF training procedure is performed with the on-the-fly training module [25,44] in VASP for primitive unit cell. The MLFF potential is constructed based on a variant of the GAP-SOAP method [30,45] with a Gaussian width of 0.5 Å. The local atomic configurations are described within a cutoff radius of 8 and 5 Å for the two- and three-body terms, respectively. The canonical ensemble (NVT) was utilized in the MD simulations, with temperature oscillations being controlled by the Langevin thermostat [46–48], at around 200 K. The phonon calculations are carried out by frozen-phonon method with VASP+phonopy [49,50], where a 2 × 2 × 2 super-cell is used, with the energy convergence threshold set as 10^{-8} eV.

For the ACE scheme, all DFT-related calculations are performed with Quantum ESPRESSO (QE) [51] to prepare the training data set: QEset. The plane-wave kinetic energy cutoff is set to 60 Ry (~816 eV) with a density cutoff of 240 Ry (~3265 eV) and shifted 4 × 4 × 4 Monkhorst–Pack meshes are used to perform Brillouin zone integration to ensure the convergence. The total energy convergence is set to be better than 10^{-14} Ry (~1.4×10^{-13} eV). Ionized pseudopotentials with the configuration $(3p)^{6.0}(4s)^{0.0}(3d)^{0.0}$ generated with the Troullier-Martins [52] method, as well as the phonon dispersion from density functional perturbation theory (DFPT) are taken from Ref. [53]. The MLFF descriptors and kernel are derived with the on-the-fly MLFF software flare [54]. The ACE-based local atomic configurations are described with a species-pair specified cutoff radius of 4.3, 5.0, and 5.0 Å for C–C, C-K, and K-K pair respectively, optimized by maximizing the log marginal likelihood (see Fig. S1). The MD for this scheme is carried out by LAMMPS [55], where NVT with Nosé–Hoover thermostat [56, 57] is set at 200 K.

The classical MD is performed for K_3C_{60} using a hybrid potential pair style, with Tersoff potential [58] applied for C–C pair and Lennard-Jones potential [59] applied for the rest pairs. To validate how well the MLFF can reproduce DFT energy and force calculated, we generate 1000 randomly distorted structures (TESTset) by phonopy, with the distortion magnitude 0.06 a.u. (~0.03 Å) for each atom.

4. Results and discussion

We have successfully generated the MLFF for K_3C_{60} with both ACE and SOAP schemes, based on which the thermal dynamics are analyzed. To further discuss the results, the trained MLFFs must be first validated. Validation checks involve the ability of trained force fields to reproduce dynamic properties obtained by DFT calculations. For quantifying the deviation, we employ two of the most commonly used metrics, the mean absolute error (MAE) and the root mean square error (RMSE) [35]:

$$\mathrm{MAE}=\frac{1}{N}\sum_i\left|y_i-\hat{y}_i\right| \tag{7}$$

$$\mathrm{RMSE} = \sqrt{\frac{1}{N}\sum_i (y_i - \hat{y}_i)^2}, \tag{8}$$

where y_i is the reference value while $\hat{y}_i$ is calculated or predicted value from MLFF model. Depending on the definition of index i, the two metrics can represent the numerical error of different properties. For example, suppose i represents the number of training steps in one MLFF procedure, the MAE and RMSE refer to the estimated Bayesian error of a specific property, which is the analysis of the intrinsic numerical error of the MLFF method itself. If the i index distinguishes the value from different methods, MAE and RMSE refer to the second aspect of the validation, which represents the errors of the comparison between the reference value (the data from DFT in MLFF) and the prediction from MLFF. In the MLFF method, y quantity usually represents energy, forces, and stress. These two metrics are suitable for all the properties in the MLFF calculations, not just for scalar quantities, such as the total energy, but vector quantities, like the force vector and the atomic displacement vector, if their norms are involved. However, there are several ways to convert vectors into norms, such as L1 norm, L2 norm, etc. L2 norm will be employed in this paper because of the error metric of the rotational invariance. In lattice dynamics, the forces or displacements are described by the force vector or normal modes, composed of all three components of each atom's force or displacement vector. Thus, the L2 norm of a force vector is calculated as

$$\|\mathbf{F}\|_2 = \sqrt{\sum_j \sum_\alpha \|F_{j,\alpha}\|_2}, \tag{9}$$

where $F_{j,\alpha}$ is the α component in the Cartesian coordinate (x, y, z) of the jth atom. This quantity characterizes the magnitude of the deviation. However, vectors possess both magnitude and direction. To account for the deviation of the directions, we construct the force vector angle Θ_y:

$$\cos(\Theta_F) = \frac{\mathbf{F}^{MLFF} \cdot \mathbf{F}^{DFT}}{|\mathbf{F}^{MLFF}| \cdot |\mathbf{F}^{DFT}|} \tag{10}$$

4.1. Efficiency and error analysis

The self-evaluation of the training errors is summarized in Fig. 1(a) and (b) for SOAP and ACE, respectively. The error analysis is based on force (SOAP) and energy (ACE). All the configurations from MD steps with a variable larger than the threshold will be sent for DFT calculations, from which the energy, force, and stress will be added to the training dataset. The threshold for force will evolve with the increase of the number of MD steps while it is kept constant for the energy. In both cases, the variables decrease with more MD steps, enhancing the training model's accuracy. The accuracy can reach 0.02 eV/Å and 0.0002 eV for the two methods, showing that the trained model can reproduce the force or energy from DFT calculations with an error within 0.02 eV/Å and 0.0002 eV, which is compatible with the relaxation procedure for the phonon calculations with DFT. On the other hand, the number of effective DFT calculations from the two schemes is 95 and 70, meaning that only 95 and 70 configurations are necessary to train an MLFF with the same level of accuracy. This shows another potential direction to enhance the efficiency of MLFF.

Fig. 1(c) summarizes the time consumed in these two schemes for phonon calculations. It is clearly shown that the time elapsed for MLFF training are similar from ACE and SOAP schemes. This is reasonable as in these two schemes, similar DFT steps are involved, 95 and 70 for QE and VASP. While there is a significant difference (about six times) between the time consumed for phonon calculations at DFT level because of the different methods for phonon calculations in QE and VASP. With QE, DFPT is employed while with VASP finite displacement method with a super-cell of $2 \times 2 \times 2$ is used, which increases the computational work load. Another reason may come from the incompatibility between the DFT and MD codes, and the phonon calculation methods at DFT level. In the ACE frame work, the MD is performed by LAMMPS while

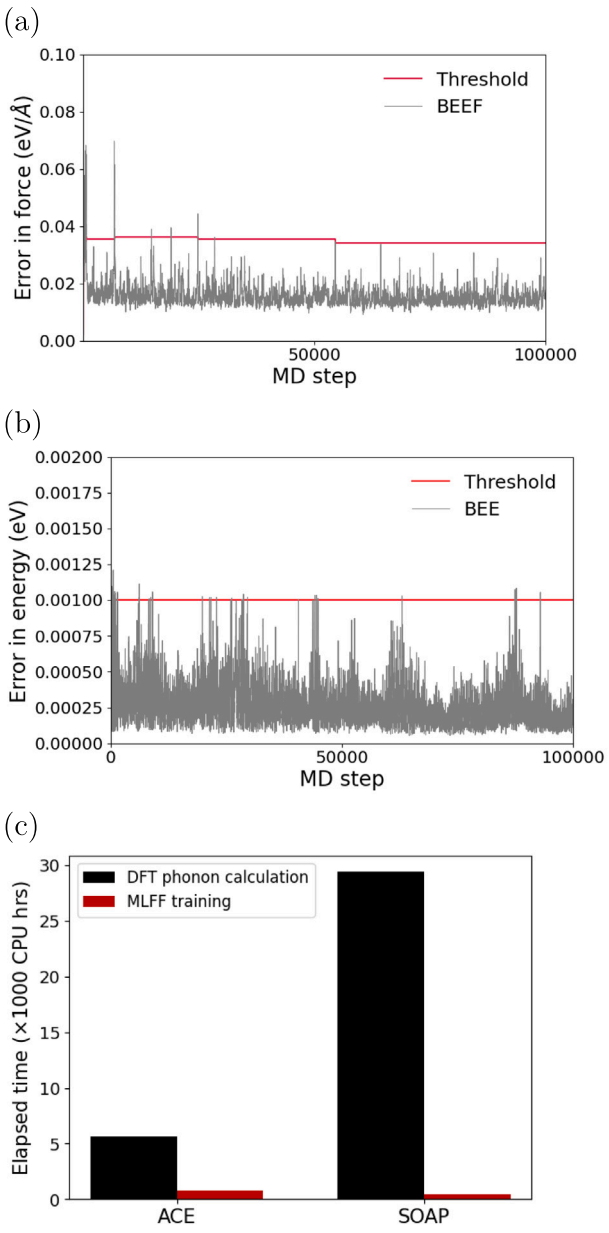

Fig. 1. Self-estimation error of MLFF in SOAP (a) and ACE (b) schemes. The time-consuming of the phonon calculations (c).

the build-in MD code in VASP is employed in SOAP scheme, resulting in more compatibility in SOAP than that in ACE. The final efficiency enhancement are about 5 times faster for ACE and 30 times faster for SOAP. However, in reality, phonon dispersion calculations at the DFT level may take a longer time since the validation of phonon dispersion, especially in the elimination of imaginary phonon frequencies as this could only be carried out after obtaining the interatomic force constants (IFCs), involving several relaxation procedures and a bunch of SCF calculations. For example, for the calculation of phonon dispersion of the K_3C_{60} from DFPT, various parameters (ENCUT/BZ sampling) were varied, and three relaxation procedures were performed to get the phonon dispersion without imaginary frequencies. And phonon calculation using force fields from MLFF training takes no time. Thus, the efficiency enhanced by the MLFF method is estimated to be at least 10 times with ACE method taking into consideration of one time imaginary elimination procedure.

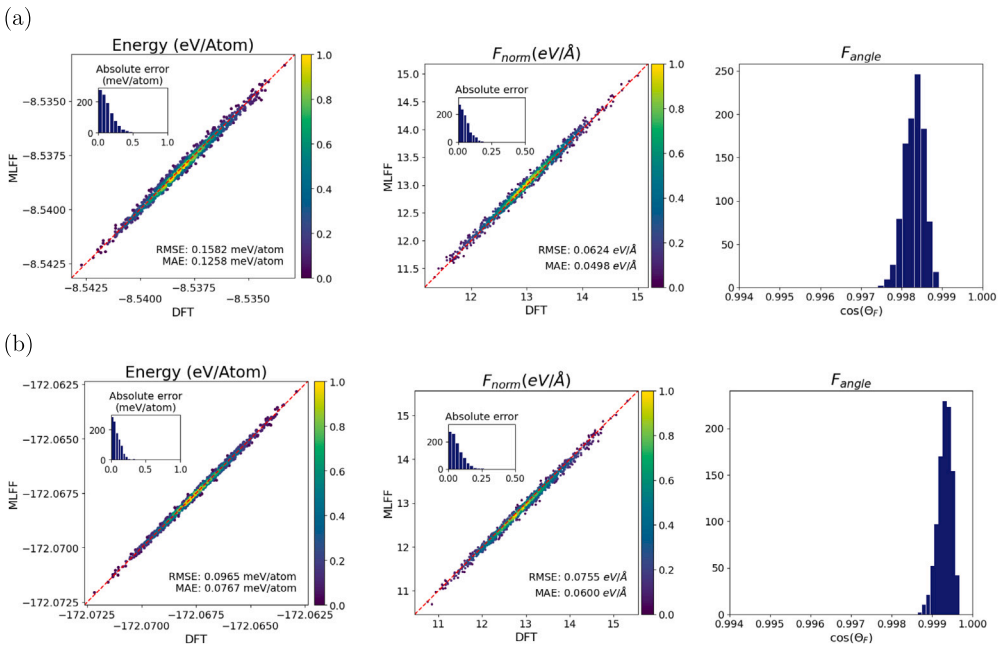

Fig. 2. Comparison of the total energy, forces between DFT calculation and the MLFF methods for both SOAP (a) and ACE (b) schemes, color-coded by Gaussian Kernel Density Estimation (KDE), rescaled to [0,1].

4.2. Validation of force field

The DFT calculations are carried out on the same TESTset by VASP and QE, of which the energy and force are compared to that from MLFF predictions with the SOAP (VASP) method and ACE (QE) method, as shown in Fig. 2(a) and (b), respectively. The figure shows clearly that MLFF from both ACE and SOAP schemes can reproduce the DFT energy and force (both the magnitude and angle). The RMSE for energy is 0.1582 and 0.0965 meV/atom for SOAP and ACE, respectively, with MAE 0.1258 and 0.0767 meV/atom, while for forces, the RMSE are 0.0624 and 0.0755 eV/Å for SOAP and ACE respectively, with MAE 0.0498 and 0.0600 eV/Å, showing the better performance of ACE than that of SOAP, which is also confirmed by the $\cos(\Theta_F)$.

The different behavior of these validation between QE and VASP is mainly because of the intrinsic features of these two software in practice. On the one hand, in principle, these two schemes are equivalent if the high enough order of the descriptors could be generated, which is impossible in reality. On the other, the DFT calculations from VASP and QE on the same TESTset are consistent as they give the same energy range, about 10 meV/Atom, and force magnitude range, about 5 eV/Å, which aligns with the benchmarks [60]. A further proof can be verified when cross check of the phonon dispersion by switching the training data set in these two methods is performed, as shown in the next section.

4.3. Phonon dispersions

With the trained force field, the interatomic force constant (IFCs) are calculated, based on which the phonon dispersion is obtained, as shown in Fig. 3, where black and red lines represent the phonon band structures calculated using DFT and the Machine Learning Force Field (MLFF) method, respectively. Specifically, the Density Functional Perturbation Theory (DFPT) method is used in QE, while the finite displacement method (FDM) is employed in the framework of VASP+phonopy for phonon calculations. To have a more complete comparison, classic molecular dynamic calculation is also carried out (Fig. 3(a) yellow line).

An overall agreement presents between the DFT data and that from MLFF can be seen in Fig. 3. However, there are some mismatches between DFT and MLFF methods, especially for the dispersions between 1050 to 1150 cm^{-1}. Besides, the optical modes from DFT are more dispersive than MLFF's. This is reasonable as the molecular feature of C_{60} is kept in K_3C_{60}. Thus, the optical modes mainly correspond to the vibrations of C_{60} molecules modified by the weak elastic interactions between C_{60} molecules. These weak elastic interactions that are of long-range nature can be accounted for by DFT method, while the MLFF is limited due to the radius cutoff of the descriptors, which are 5.0 Å (3-body radius cutoff for SOAP) and 4.3 Å (C-C radius cutoff for ACE), smaller than the diameter of C_{60} molecule (~7.0 Å) [61]. The classic molecular dynamic method gives a larger mismatch in that it predicts the highest phonon frequency is 1923 cm^{-1}, while that from both the DFT and MLFF is around 1500 cm^{-1}. In the low energy region (below 300 cm^{-1}, Fig. 3(b)), the acoustic phonons are poorly reproduced with SOAP scheme compared with that by ACE. However the imaginary dispersions calculated by FDM with VASP are captured by the MLFF method.

Table 2
P_{RMSE} for phonon calculations for the low energy (P^L_{RMSE}), high energy (P^H_{RMSE}) and full energy (P^F_{RMSE}) regions with different methods.

	DFTData	P^L_{RMSE}	P^H_{RMSE}	P^F_{RMSE}
ACE	QE	8.70	10.79	10.56
	VASP	26.56	15.50	16.98
SOAP	QE	8.50	10.70	10.49
	VASP	26.92	15.07	16.72
MD		87.49	221.32	210.60

To quantitatively describe the difference between DFT and MLFF phonons, we defined the root mean square error for phonon calculations (P_{RMSE}):

$$P_{\mathrm{RMSE}} = \sqrt{\sum_{\mathbf{q}} \sum_{\gamma=1}^{N_{mode}} \frac{(\omega^{\mathrm{MLFF}}_{\mathbf{q}\gamma} - \omega^{\mathrm{DFT}}_{\mathbf{q}\gamma})^2}{N_{mode} \times N_{\mathbf{q}}}}, \tag{11}$$

where $N_{\mathbf{q}}$ is the number of $\mathbf{q}$ points along high-symmetry path in the Brillouin, N_{mode} represents the number of modes in the high/low/all

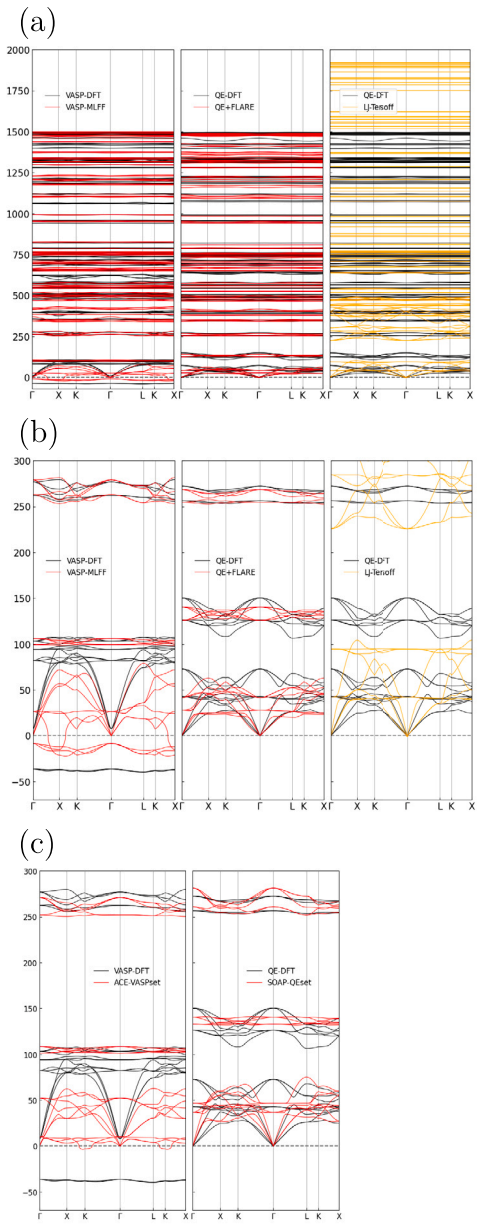

Fig. 3. Phonon dispersion (cm^{-1}) from DFT(black) and MLFF(red) calculated by QEflare and VASP, as well as the classic molecular dynamics method (Tersoff+LJ, yellow solid line). (a). full phonon dispersions, (b). phonon dispersion in the low energy region (below 300 cm^{-1}). (c). Cross-check of the training with SOAP and ACE schemes the same DFT data sets on different schemes in the low energy region, referring Fig. S2 for the full comparison.

energy regions. P_{RMSE} are summarized in Table 2. The P^{L}_{RMSE} and P^{H}_{RMSE} represents the RMSE of the phonon dispersions in the low energy region (below 300 cm^{-1}) and the high energy region (above 300 cm^{-1}). The P^{L}_{RMSE} are 26.92, 8.70, and 87.49 for SOAP, ACE, and MD methods, respectively, while P^{H}_{RMSE} are 15.07, 10.79, and 221.32 for SOAP, ACE and MD method. This complies with the fact that the descriptors are local, and shows the necessity to include the semi-local or non-local interaction to improve phonon predictions with MLFF.

As C_{60} is an ideal platform for studying the Jahn-Teller effect and Jahn-Teller plays an important role in K_3C_{60}, we compare the Jahn-Teller related frequencies from DFT and MLFF method, as shown in Table 3. Due to the selection rule, only five-fold degenerate H_g modes of C_{60} [53] are Jahn-Teller active. The H_g modes are split into

Table 3
Comparison of phonon frequencies (cm^{-1}) of H_g modes at the Γ point from DFPT, FDM, MLFF with ACE and SOAP, as well as experimental data.

Mode	DFPT (QE)		MLFF (ACE)		FDM (VASP)		MLFF (SOAP)		Exp. [62]
	E_g	T_g	E_g	T_g	E_g	T_g	E_g	T_g	
$H_g(1)$	257	274	255	268	262	277	263	279	268
$H_g(2)$	406	401	417	401	399	398	383	384	416
$H_g(3)$	637	642	650	652	621	625	654	654	712
$H_g(4)$	770	768	757	755	760	760	768	765	752
$H_g(5)$	1094	1087	1098	1093	1064	1060	1102	1099	–
$H_g(6)$	1251	1240	1222	1221	1214	1207	1231	1229	–
$H_g(7)$	1357	1353	1350	1336	1333	1338	1332	1334	1409
$H_g(8)$	1499	1497	1480	1479	1488	1488	1478	1477	1550

two-fold degenerate E_g and three-fold degenerate T_{3g} modes as the symmetry is lowered from I_h to T_h. The difference between calculated and experimental data is within 10%, indicating the good performance of MLFF.

4.4. Cross training

As discussed in Section 2.1, the two schemes of SOAP and ACE are equivalent when a higher order of basis set is included. In contrast, Fig. 3 shows imaginary frequencies with the SOAP scheme, while no imaginary frequencies appear with ACE. To clarify the primary origin of the difference, we perform a cross-check validation by switching the training data for SOAP and ACE. The phonon dispersion in the low energy region is displayed in Fig. 3(c), with the full comparison presented in Fig. S2. When applying the SOAP scheme to the QE set, imaginary frequencies are eliminated, and the dispersion, particularly in the low energy region, replicates that from the ACE scheme. Conversely, when inputting the VASP set into the ACE scheme, imaginary frequencies appear. This indicates that the phonon dispersion and dynamic properties heavily rely on the DFT calculations. The overall P_{RMSE} values are 10.49 and 16.98, with P^{L}_{RMSE} values of 8.50 and 26.56, and P^{H}_{RMSE} values of 10.70 and 15.50, respectively.

4.5. Elastic moduli

The trained force field is further utilized to predict the elastic moduli. For FCC crystals, the three independent components of the elastic moduli: C_{xxxx}, C_{xxyy}, and C_{xyxy} [63], are calculated using DFT, MLFF, and classical MD, with the results summarized in Table 4. As shown in the table, the MLFF predictions can deviate from the DFT reference values by several hundred kBar. This discrepancy, while significant, offers valuable insight into areas for future model refinement and is likely attributed to two aspects. The first one is high sensitivity to prediction errors. Elastic moduli are derivatives of stresses σ with respect to strain ε ($C_{ij} = \partial\sigma_i/\partial\varepsilon_j$), where minor inaccuracies in the predicted stresses can be significantly amplified when calculating the moduli. The use of FDM that derives moduli from a sparse set of discrete strains also leaves a tiny room to allow any random errors to average out. While both training schemes only include stress at most into the training scheme, the accuracy in elastic moduli is not guaranteed. In addition, sufficient sampling of the configuration space is lacking. The model is trained primarily on a MD simulations which may only explore the PES around equilibrium structure, without sufficiently sampling atomic configurations to include anisotropic strains that are required to derive elastic moduli. The MLFFs are therefore forced to extrapolate for the uncertain domain that leads to reduced accuracy.

Table 4
The three independent general moduli, C_{xxxx}, C_{xxyy}, and C_{xyxy} (kBar) for different methods.

	C_{xxxx}	C_{xxyy}	C_{xyxy}
QE	364.46	237.58	131.29
MLFF (flare)	76.53	39.12	123.12
VASP	124.47	266.34	15.21
MLFF (VASP)	408.11	250.88	201.12
MD[a]	489.62	222.83	101.05

[a] MD values are averages of the elastic tensor elements due to lifted degeneracy for broken FCC symmetry (See Table. S1).

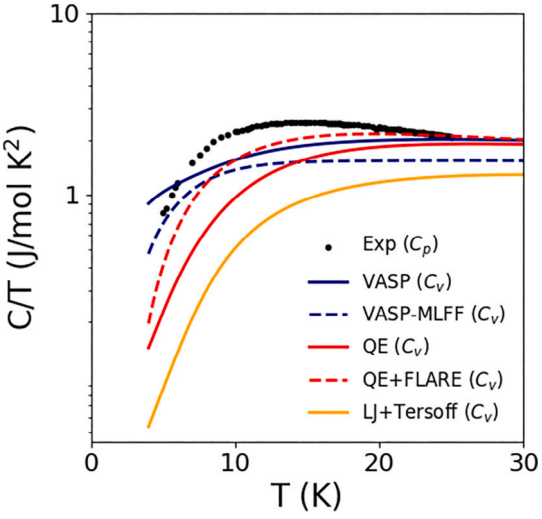

Fig. 4. Specific heat of K_3C_{60}.

4.6. Specific heat

The specific heat is produced based on phonon calculations using different methods, as shown in Fig. 4, and is compared to experimental data measured by a conventional adiabatic heat pulse method [64]. This specific heat consists of the linear-in-T term, which indicates structural disorder, a cubic Debye term with $\Theta_{Debye} = 70$ K, chosen by scaling the Debye frequency of copper by the ratio of the bulk moduli between copper and K_3C_{60}, and an Einstein term corresponding to a 34 ± 1 K level [65].

Due to the severe overestimation of phonon dispersions by the classic MD method (orange line), the specific heat calculated with MD is furthest from the experimental data. The predicted specific heat using the MLFF reproduces the temperature dependence with a slight enhancement. The results from the SOAP scheme (blue dashed line) and DFT (blue solid line) calculations intersect at $T \approx 4$ K, which should not occur since the calculated C_v should not exceed C_p. This discrepancy mainly arises from the incorrect ground state in the DFT calculations. The ACE scheme results (red dashed line) and DFPT calculations (red solid line) are reasonable; however, there remains a small mismatch, likely due to the lack of consideration for disorder in C_{60}, which exists in fullerides [66,67]. Although phonon calculations of disordered fullerides with DFT may be excessively resource-intensive, the MLFF method demonstrates potential in addressing this issue.

5. Conclusion

In this work, we present for the first time a rigorous study of the dynamic properties of the alkali-doped molecular crystal K_3C_{60} using machine learning force field (MLFF) methods with SOAP and ACE schemes. The results demonstrate that MLFF can accurately reproduce phonon dispersion patterns comparable to those obtained from DFT calculations while offering substantial improvements in computational efficiency. Based on the analysis of the training dataset, only 95 and 70 configurations are necessary for the phonon calculations, enhancing computational efficiency by about one order of magnitude. This suggests another potential direction for enhancing the efficiency of MLFF. The study confirms the suitability of MLFF approaches for investigating molecular crystals, particularly when traditional methods, such as density functional perturbation theory (DFPT), are computationally prohibitive for complex systems. A comparison of two distinct MLFF frameworks highlights the critical role that high-quality DFT training data plays in the predictive power of the MLFF. The specific heat calculated using the MLFF agrees with experimental results, further validating the reliability of the MLFF approach for thermodynamic properties.

However, the cross-check validation of the two schemes shows that although the MLFF engine can achieve the accuracy of DFT calculations for dynamic properties, it relies heavily on the DFT training data. Besides, the force field in this paper is specified to the K_3C_{60}. Typically, a force field trained on one specific material is tailored to accurately reproduce the properties of that material alone. Even when the training is performed for a particular phase, transferring the potential to other phases of the same material remains difficult. To address this, there is a growing trend toward developing so-called "universal" force fields for individual elements [68,69]. Besides, there is a very recent work on the universal foundation of transfer training for molecular crystals, but lattice dynamics is not well studied [70]. However, we believe that constructing truly universal force fields is ultimately unfeasible, as it may lead to issues similar to those encountered in the development of pseudopotentials in DFT. Instead, we propose to develop a locally transferable force field tailored to a family of related materials. For example, it is more feasible to reach the transferability for the force field to K_nC_{60} (n=1,2, …,6) family with the training performed on K_3C_{60}. Therefore, exploring how to surpass this limitation and maximize transferability may be an important topic for future work.

CRediT authorship contribution statement

Ran Mo: Writing – original draft, Visualization, Validation, Software, Methodology, Investigation, Formal analysis, Data curation. **Zhishuo Huang:** Writing – review & editing, Writing – original draft, Supervision, Investigation, Funding acquisition, Formal analysis, Conceptualization. **Liviu Ungur:** Writing – review & editing, Writing – original draft, Validation, Supervision, Resources, Project administration, Methodology, Funding acquisition, Conceptualization.

Declaration of competing interest

The authors declare no competing financial interest.

Acknowledgments

Z.H. and L.U. acknowledge the National University of Singapore, Singapore for financing research projects A-8000079-00-00, and A-8001894-00-00 (MOE Tier 2 programme, T2EP10123-0018). R.M. is supported by the NUS Research Scholarship program. Ab initio calculations were performed on the ASPIRE-2A cluster (www.nscc.sg) under projects 11001278, 11003762, 51000267, and 11003763. This work used computational resources of the supercomputer Fugaku provided by RIKEN/NSCC through the HPCI System Research Project (Project ID: hp240202). The computational resources of the HPC-NUS are gratefully acknowledged.

Appendix A. Supplementary data

Supplementary material related to this article can be found online at https://doi.org/10.1016/j.chphi.2025.100931.

Data availability

All the available data is deposited in Materials Cloud with the link: https://doi.org/10.24435/materialscloud:py-bf.

References

[1] Y. Wang, S.-L. Shang, H. Fang, Z.-K. Liu, L.-Q. Chen, First-principles calculations of lattice dynamics and thermal properties of polar solids, Npj Comput. Mater. 2 (1) (2016) http://dx.doi.org/10.1038/npjcompumats.2016.6.

[2] M.T. Dove, Introduction to Lattice Dynamics, Cambridge Topics in Mineral Physics and Chemistry, Cambridge University Press, Cambridge, 1993, http://dx.doi.org/10.1017/CBO9780511619885.

[3] G. Ding, G. Gao, Z. Huang, W. Zhang, K. Yao, Thermoelectric properties of monolayer mse2 (m=zr, hf): low lattice thermal conductivity and a promising figure of merit, Proc. Spie 27 (37) (2016) 375703, http://dx.doi.org/10.1088/0957-4484/27/37/375703.

[4] M. Born, K. Huang, Dynamical Theory of Crystal Lattices, Oxford University Press, London, 1996.

[5] M. Holynska, Single-Molecule Magnets: Molecular Architectures and Building Blocks for Spintronics, John Wiley & Sons, Weinheim, 2019.

[6] G. Olle, Alkali-Doped Fullerides: Narrow-Band Solids with Unusual Properties, World Scientific Publishing Company, Singapore, 2004.

[7] A.K. Geim, I.V. Grigorieva, Van der waals heterostructures, Nature 499 (7459) (2013) 419–425, http://dx.doi.org/10.1038/nature12385.

[8] R.M. Martin, Electronic Structure: Basic Theory and Practical Methods, Cambridge University Press, New York, 2020.

[9] S.G. Volz, G. Chen, Molecular-dynamics simulation of thermal conductivity of silicon crystals, Phys. Rev. B 61 (4) (2000) 2651–2656, http://dx.doi.org/10.1103/PhysRevB.61.2651.

[10] A.J.H. McGaughey, J.M. Larkin, Predicting phonon properties from equilibrium molecular dynamics simulations, Annu. Rev. Heat Transf. 17 (2014) 49–87.

[11] D. Marx, J. Hutter, Ab Initio Molecular Dynamics: Basic Theory and Advanced Methods, Cambridge University Press, Cambridge, 2009, http://dx.doi.org/10.1017/CBO9780511609633.

[12] S. Baroni, S. de Gironcoli, A. Dal Corso, P. Giannozzi, Phonons and related crystal properties from density-functional perturbation theory, Rev. Modern Phys. 73 (2) (2001) 515–562, http://dx.doi.org/10.1103/RevModPhys.73.515.

[13] X. Gonze, C. Lee, Dynamical matrices, born effective charges, dielectric permittivity tensors, and interatomic force constants from density-functional perturbation theory, Phys. Rev. B 55 (16) (1997) 10355–10368, http://dx.doi.org/10.1103/PhysRevB.55.10355.

[14] G. Kresse, J. Furthmüller, J. Hafner, Ab initio force constant approach to phonon dispersion relations of diamond and graphite, Europhys. Lett. 32 (9) (1995) 729–734, http://dx.doi.org/10.1209/0295-5075/32/9/005.

[15] A. Gavezzotti, Molecular Aggregation: Structure Analysis and Molecular Simulation of Crystals and Liquids, Oxford University Press, 2006, http://dx.doi.org/10.1093/acprof:oso/9780198570806.001.0001.

[16] V.I. Anisimov, J. Zaanen, O.K. Andersen, Band theory and mott insulators: Hubbard u instead of stoner i, Phys. Rev. B 44 (3) (1991) 943–954, http://dx.doi.org/10.1103/PhysRevB.44.943.

[17] S.L. Dudarev, G.A. Botton, S.Y. Savrasov, C.J. Humphreys, A.P. Sutton, Electron-energy-loss spectra and the structural stability of nickel oxide: An lsda+u study, Phys. Rev. B 57 (3) (1998) 1505–1509, http://dx.doi.org/10.1103/PhysRevB.57.1505.

[18] V.I. Anisimov, F. Aryasetiawan, A.I. Lichtenstein, First-principles calculations of the electronic structure and spectra of strongly correlated systems: the lda+u method, J. Phys.: Condens. Matter. 9 (4) (1997) 767–808, http://dx.doi.org/10.1088/0953-8984/9/4/002.

[19] S. Grimme, J. Antony, S. Ehrlich, H. Krieg, A consistent and accurate ab initio parametrization of density functional dispersion correction (dft-d) for the 94 elements h-pu, J. Chem. Phys. 132 (15) (2010) 154104, http://dx.doi.org/10.1063/1.3382344.

[20] S. Grimme, Semiempirical gga-type density functional constructed with a long-range dispersion correction, J. Comput. Chem. 27 (15) (2006) 1787–1799, http://dx.doi.org/10.1002/jcc.20495.

[21] M. Dion, H. Rydberg, E. Schroder, D.C. Langreth, B.I. Lundqvist, Van der waals density functional for general geometries, Phys. Rev. Lett. 92 (24) (2004) 246401, http://dx.doi.org/10.1103/PhysRevLett.92.246401.

[22] A. Seko, A. Togo, H. Hayashi, K. Tsuda, L. Chaput, I. Tanaka, Prediction of low-thermal-conductivity compounds with first-principles anharmonic lattice-dynamics calculations and bayesian optimization, Phys. Rev. Lett. 115 (20) (2015) http://dx.doi.org/10.1103/PhysRevLett.115.205901.

[23] Z. Chen, N. Andrejevic, T. Smidt, Z. Ding, Q. Xu, Y.T. Chi, Q.T. Nguyen, A. Alatas, J. Kong, M. Li, Direct prediction of phonon density of states with euclidean neural networks, Adv Sci (Weinh) 8 (12) (2021) e2004214, http://dx.doi.org/10.1002/advs.202004214.

[24] Y. Zhang, H. Wang, W. Chen, J. Zeng, L. Zhang, H. Wang, W. E, Dp-gen: A concurrent learning platform for the generation of reliable deep learning based potential energy models, Comput. Phys. Comm. 253 (2020) http://dx.doi.org/10.1016/j.cpc.2020.107206.

[25] R. Jinnouchi, J. Lahnsteiner, F. Karsai, G. Kresse, M. Bokdam, Phase transitions of hybrid perovskites simulated by machine-learning force fields trained on the fly with bayesian inference, Phys. Rev. Lett. 122 (22) (2019) 225701, http://dx.doi.org/10.1103/PhysRevLett.122.225701.

[26] V.V. Ladygin, P.Y. Korotaev, A.V. Yanilkin, A.V. Shapeev, Lattice dynamics simulation using machine learning interatomic potentials, Nato. Sc. S. Ss. Iii. C. S. 172 (2020) http://dx.doi.org/10.1016/j.commatsci.2019.109333.

[27] R. Drautz, Atomic cluster expansion for accurate and transferable interatomic potentials, Phys. Rev. B 99 (1) (2019) http://dx.doi.org/10.1103/PhysRevB.99.014104, drautz, Ralf Drautz, Ralf/A-2938-2017 Drautz, Ralf/0000-0001-7101-8804 2469-9969.

[28] O. Gunnarsson, Superconductivity in fullerides, Rev. Modern Phys. 69 (2) (1997) 575–606.

[29] M. Mitrano, A. Cantaluppi, D. Nicoletti, S. Kaiser, A. Perucchi, S. Lupi, P. Di Pietro, D. Pontiroli, M. Riccò, S.R. Clark, D. Jaksch, A. Cavalleri, Possible light-induced superconductivity in k3c60 at high temperature, Nature 530 (7591) (2016) 461–+, http://dx.doi.org/10.1038/nature16522.

[30] A.P. Bartók, R. Kondor, G. Csányi, On representing chemical environments, Phys. Rev. B 87 (18) (2013) http://dx.doi.org/10.1103/PhysRevB.87.184115.

[31] F. Musil, A. Grisafi, A.P. Bartók, C. Ortner, G. Csányi, M. Ceriotti, Physics-inspired structural representations for molecules and materials, Chem. Rev. 121 (16) (2021) 9759–9815, http://dx.doi.org/10.1021/acs.chemrev.1c00021.

[32] C.D. Taylor, Connections between the energy functional and interaction potentials for materials simulations, Phys. Rev. B 80 (2) (2009) http://dx.doi.org/10.1103/PhysRevB.80.024104.

[33] C.K. Williams, C.E. Rasmussen, Gaussian Processes for Machine Learning, vol. 2, MIT press Cambridge, MA, 2006.

[34] S. De, A.P. Bartók, G. Csányi, M. Ceriotti, Comparing molecules and solids across structural and alchemical space, Phys. Chem. Chem. Phys. 18 (20) (2016) 13754–13769, http://dx.doi.org/10.1039/c6cp00415f.

[35] J.D. Morrow, J.L.A. Gardner, V.L. Deringer, How to validate machine-learned interatomic potentials, J. Chem. Phys. 158 (12) (2023) 121501, http://dx.doi.org/10.1063/5.0139611.

[36] M. Abramowitz, I.A. Stegun, Handbook of mathematical functions with formulas, graphs, and mathematical tables, vol. 55, US Government printing office, Washington, 1972.

[37] K. Tanigaki, I. Hirosawa, T.W. Ebbesen, J. Mizuki, Shimakawa, Y. Kubo, J.S. Tsai, S. Kuroshima, Superconductivity in sodium-and lithium-containing alkali-metal fullerides, Nature 356 (6368) (1992) 419–421, http://dx.doi.org/10.1038/356419a0.

[38] G. Kresse, J. Hafner, Ab initio molecular dynamics for liquid metals, Phys. Rev. B 47 (1) (1993) 558–561, http://dx.doi.org/10.1103/PhysRevB.47.558.

[39] G. Kresse, J. Furthmüller, Efficient iterative schemes for ab initio total-energy calculations using a plane-wave basis set, Phys. Rev. B 54 (16) (1996) 11169–11186, http://dx.doi.org/10.1103/PhysRevB.54.11169.

[40] H.J. Monkhorst, J.D. Pack, Special points for brillouin-zone integrations, Phys. Rev. B 13 (12) (1976) 5188–5192, http://dx.doi.org/10.1103/PhysRevB.13.5188.

[41] G. Kresse, D. Joubert, From ultrasoft pseudopotentials to the projector augmented-wave method, Phys. Rev. B 59 (3) (1999) 1758–1775, http://dx.doi.org/10.1103/PhysRevB.59.1758.

[42] P.E. Blöchl, Projector augmented-wave method, Phys. Rev. B 50 (24) (1994) 17953–17979, http://dx.doi.org/10.1103/PhysRevB.50.17953.

[43] J.P. Perdew, K. Burke, M. Ernzerhof, Generalized gradient approximation made simple, Phys. Rev. Lett. 77 (18) (1996) 3865–3868.

[44] R. Jinnouchi, F. Karsai, G. Kresse, On-the-fly machine learning force field generation: Application to melting points, Phys. Rev. B 100 (1) (2019) http://dx.doi.org/10.1103/PhysRevB.100.014105.

[45] A.P. Bartók, M.C. Payne, R. Kondor, G. Csányi, Gaussian approximation potentials: The accuracy of quantum mechanics, without the electrons, Phys. Rev. Lett. 104 (13) (2010) http://dx.doi.org/10.1103/PhysRevLett.104.136403.

[46] M. Allen, D. Tildesley, Computer Simulation of Liquids, Computer Simulation of Liquids, Clarendon Press, Oxford, 1989.

[47] W.G. Hoover, A.J.C. Ladd, B. Moran, High-strain-rate plastic flow studied via nonequilibrium molecular dynamics, Phys. Rev. Lett. 48 (1982) 1818–1820, http://dx.doi.org/10.1103/PhysRevLett.48.1818.

[48] D.J. Evans, Computer experiment for nonlinear thermodynamics of couette flow, J. Chem. Phys. 78 (6) (1983) 3297–3302, http://dx.doi.org/10.1063/1.445195.

[49] A. Togo, I. Tanaka, First principles phonon calculations in materials science, Scr. Mater. 108 (2015) 1–5, http://dx.doi.org/10.1016/j.scriptamat.2015.07.021.

[50] A. Togo, L. Chaput, T. Tadano, I. Tanaka, Implementation strategies in phonopy and phono3py, J. Phys.: Condens. Matter. 35 (35) (2023) http://dx.doi.org/10.1088/1361-648X/acd831.

[51] P. Giannozzi, O. Andreussi, T. Brumme, O. Bunau, M. Buongiorno Nardelli, M. Calandra, R. Car, C. Cavazzoni, D. Ceresoli, M. Cococcioni, N. Colonna, I. Carnimeo, A. Dal Corso, S. de Gironcoli, P. Delugas, R.A. DiStasio, A. Ferretti, A. Floris, G. Fratesi, G. Fugallo, R. Gebauer, U. Gerstmann, F. Giustino, T. Gorni, J. Jia, M. Kawamura, H.Y. Ko, A. Kokalj, E. Küçükbenli, M. Lazzeri, M. Marsili, N. Marzari, F. Mauri, N.L. Nguyen, H.V. Nguyen, A. Otero-de-la Roza, L. Paulatto, S. Poncé, D. Rocca, R. Sabatini, B. Santra, M. Schlipf, A.P. Seitsonen, A. Smogunov, I. Timrov, T. Thonhauser, P. Umari, N. Vast, X. Wu, S. Baroni, Advanced capabilities for materials modelling with quantum espresso, J. Phys.: Condens. Matter. 29 (46) (2017) 465901, http://dx.doi.org/10.1088/1361-648X/aa8f79.

[52] N. Troullier, J.L. Martins, Efficient pseudopotentials for plane-wave calculations, Phys. Rev. B 43 (1991) 1993–2006, http://dx.doi.org/10.1103/PhysRevB.43.1993.

[53] Z. Huang, M.D. Albaqami, T. Sato, N. Iwahara, L.F. Chibotaru, Jahn-Teller effect in the cubic fullerides A_3C_{60}, Phys. Rev. B 103 (13) (2021) 134102, http://dx.doi.org/10.1103/PhysRevB.103.134102.

[54] J. Vandermause, S.B. Torrisi, S. Batzner, Y. Xie, L. Sun, A.M. Kolpak, B. Kozinsky, On-the-fly active learning of interpretable bayesian force fields for atomistic rare events, Npj Comput. Mater. 6 (1) (2020) http://dx.doi.org/10.1038/s41524-020-0283-z.

[55] A.P. Thompson, H.M. Aktulga, R. Berger, D.S. Bolintineanu, W.M. Brown, P.S. Crozier, P.J. in 't Veld, A. Kohlmeyer, S.G. Moore, T.D. Nguyen, R. Shan, M.J. Stevens, J. Tranchida, C. Trott, S.J. Plimpton, Lammps - a flexible simulation tool for particle-based materials modeling at the atomic, meso, and continuum scales, Comput. Phys. Comm. 271 (2022) 108171, http://dx.doi.org/10.1016/j.cpc.2021.108171.

[56] S. Nose, A unified formulation of the constant temperature molecular-dynamics methods, J. Chem. Phys. 81 (1) (1984) 511–519, http://dx.doi.org/10.1063/1.447334.

[57] W.G. Hoover, Canonical dynamics: Equilibrium phase-space distributions, Phys. Rev. A 31 (1985) 1695–1697, http://dx.doi.org/10.1103/PhysRevA.31.1695.

[58] J. Tersoff, Modeling solid-state chemistry: Interatomic potentials for multicomponent systems, Phys. Rev. B 39 (1989) 5566–5568, http://dx.doi.org/10.1103/PhysRevB.39.5566.

[59] J.E. Jones, S. Chapman, On the determination of molecular fields.—i. from the variation of the viscosity of a gas with temperature, Proc. R. Soc. Lond. A 106 (738) (1924) 441–462, http://dx.doi.org/10.1098/rspa.1924.0081, arXiv:https://royalsocietypublishing.org/doi/pdf/10.1098/rspa.1924.0081.

[60] K. Lejaeghere, G. Bihlmayer, T. Björkman, P. Blaha, S. Blügel, V. Blum, D. Caliste, I.E. Castelli, S.J. Clark, A. Dal Corso, S. de Gironcoli, T. Deutsch, J.K. Dewhurst, I. Di Marco, C. Draxl, M. Dułak, O. Eriksson, J.A. Flores-Livas, K.F. Garrity, L. Genovese, P. Giannozzi, M. Giantomassi, S. Goedecker, X. Gonze, O. Grånäs, E.K.U. Gross, A. Gulans, F. Gygi, D.R. Hamann, P.J. Hasnip, N.A.W. Holzwarth, D. Iusan, D.B. Jochym, F. Jollet, D. Jones, G. Kresse, K. Koepernik, E. Küçükbenli, Y.O. Kvashnin, I.L.M. Locht, S. Lubeck, M. Marsman, N. Marzari, U. Nitzsche, L. Nordström, T. Ozaki, L. Paulatto, C.J. Pickard, W. Poelmans, M.I.J. Probert, K. Refson, M. Richter, G.M. Rignanese, S. Saha, M. Scheffler, M. Schlipf, K. Schwarz, S. Sharma, F. Tavazza, P. Thunström, A. Tkatchenko, M. Torrent, D. Vanderbilt, M.J. van Setten, V. Van Speybroeck, J.M. Wills, J.R. Yates, G.X. Zhang, S. Cottenier, Reproducibility in density functional theory calculations of solids, Science 351 (6280) (2016) 6280, http://dx.doi.org/10.1126/science.aad3000.

[61] O. Gunnarsson, Alkali-Doped Fullerides: Narrow-Band Solids with Unusual Properties, World Scientific, Singapore, 2004.

[62] P. Zhou, K.-A. Wang, A.M. Rao, P.C. Eklund, G. Dresselhaus, M.S. Dresselhaus, Raman-scattering studies of homogeneous K_3C_{60} films, Phys. Rev. B 45 (18) (1992) 10838–10840, http://dx.doi.org/10.1103/PhysRevB.45.10838.

[63] L.D. Landau, E.M. Lifshitz, Theory of elasticity, vol. 7, Pergamon Press, Reading, Mass; London, 1959, qA931 Lan.

[64] D. Varshney, N. Kaurav, A. Dube, R.K. Singh, Role of vibrational optical phonons in the heat capacity of k3c60, Synth. Met. 155 (2) (2005) 380–383, http://dx.doi.org/10.1016/j.synthmet.2005.09.018.

[65] A.P. Ramirez, M.J. Rosseinsky, D.W. Murphy, R.C. Haddon, Specific-heat jump at T_c and normal-state magnetic susceptibility of A_3C_{60}, Phys. Rev. Lett. 69 (11) (1992) 1687–1690, http://dx.doi.org/10.1103/PhysRevLett.69.1687, pRL.

[66] S.-Z. Wang, M.-Q. Ren, S. Han, F.-J. Cheng, X.-C. Ma, Q.-K. Xue, C.-L. Song, Merohedral disorder and impurity impacts on superconductivity of fullerenes, Commun. Phys. 4 (1) (2021) http://dx.doi.org/10.1038/s42005-021-00619-y.

[67] I. Mazin, I. I, A.I. Liechtenstein, O. Gunnarsson, O.K. Andersen, V.P. Antropov, S.E. Burkov, Orientational order in A_3C_{60}: Antiferromagnetic Ising model for the fcc lattice, Phys. Rev. Lett. 70 (26) (1993) 4142–4145, http://dx.doi.org/10.1103/PhysRevLett.70.4142.

[68] A.P. Bartók, J. Kermode, N. Bernstein, G. Csányi, Machine learning a general-purpose interatomic potential for silicon, Phys. Rev. X 8 (2018) 041048, http://dx.doi.org/10.1103/PhysRevX.8.041048.

[69] V.L. Deringer, M.A. Caro, G. Csányi, A general-purpose machine-learning force field for bulk and nanostructured phosphorus, Nat. Commun. 11 (1) (2020) 5461.

[70] M. Feng, C. Zhao, G.M. Day, X. Evangelopoulos, A.I. Cooper, A universal foundation model for transfer learning in molecular crystals, Chem. Sci. 16 (28) (2025) 12844–12859, http://dx.doi.org/10.1039/d5sc00677e, eCollection 2025 Jul 16;

Minggao Zhao feng, Chengxi Day, Graeme M. Evangelopoulos, Xenophon Cooper, Andrew i eng england 2025/06/20 , Chem. Sci. 16 (28) (2025) 12844–12859.